

# Polytropic dark halos of elliptical galaxies

Curtis J. Saxton<sup>\*</sup> and Ignacio Ferreras

*Mullard Space Science Laboratory, University College London, Holmbury St Mary, Dorking, Surrey RH5 6NT*

MNRAS Ref MN-09-2224-MJ, Revised version - January 2010

## ABSTRACT

The kinematics of stars and planetary nebulae in early type galaxies provide vital clues to the enigmatic physics of their dark matter halos. We fit published data for fourteen such galaxies using a spherical, self-gravitating model with two components: (1) a Sérsic stellar profile fixed according to photometric parameters, and (2) a polytropic dark matter halo that conforms consistently to the shared gravitational potential. The polytropic equation of state can describe extended theories of dark matter involving self-interaction, non-extensive thermostatics, or boson condensation (in a classical limit). In such models, the flat-cored mass profiles widely observed in disc galaxies are due to innate dark physics, regardless of any baryonic agitation. One of the natural parameters of this scenario is the number of effective thermal degrees of freedom of dark matter ( $F_d$ ) which is proportional to the dark heat capacity. By default we assume a cosmic ratio of baryonic and dark mass. Non-Sérsic kinematic ideosyncrasies and possible non-sphericity thwart fitting in some cases. In all fourteen galaxies the fit with a polytropic dark halo improves or at least gives similar fits to the velocity dispersion profile, compared to a stars-only model. The good halo fits usually prefer  $F_d$  values from six to eight. This range complements the recently inferred limit of  $7 < F_d < 10$  (Saxton & Wu), derived from constraints on galaxy cluster core radii and black hole masses. However a degeneracy remains: radial orbital anisotropy or a depleted dark mass fraction could shift our models' preference towards lower  $F_d$ ; whereas a loss of baryons would favour higher  $F_d$ .

**Key words:** dark matter — galaxies: elliptical — galaxies: haloes — galaxies: individual (NGC 821, NGC 1023, NGC 1344, NGC 1400, NGC 1407, NGC 3377, NGC 3379, NGC 3608, NGC 4374, NGC 4494, NGC 4564, NGC 4697, NGC 5128, NGC 5846) — galaxies: structure — stellar dynamics

## 1 INTRODUCTION

Simulations that assume simple, non-interacting dark matter successfully reproduce cosmic large-scale structure (see e.g. Springel et al. 2006). However, they also predict power-law cusps of dark density at the centres of all virialised structures (e.g. Dubinski & Carlberg 1991; Navarro et al. 1996; Moore et al. 1998; Diemand et al. 2004, 2005). Dynamical and other circumstantial evidence for many galaxy types imply cores of nearly uniform dark density (e.g. Flores & Primack 1994; Moore 1994; Burkert 1995; Weldrake et al. 2003; Gentile et al. 2004; Simon et al. 2005; de Blok 2005; Kuzio de Naray et al. 2006; Weijmans et al. 2008). It remains debatable whether the present-day cores are innate, or whether a violent, primordial form of baryonic “feedback” somehow conspired to erase (or exacerbate) all cusps (e.g.

Blumenthal et al. 1986; Gnedin & Zhao 2002; Gnedin et al. 2004; Romano-Díaz et al. 2008; Jardel & Sellwood 2009).

The observational situation in elliptical galaxies is less clear than for other morphological types, because of the relative difficulty of observing suitable kinematic tracers at a range of radii. These data may suffer degeneracies between mass profiles and the orbital anisotropies of kinematic tracers (Binney & Mamon 1982). X-ray emission (if detected) is informative if hydrostasis is a fair assumption. Observations of some X-ray emitting elliptical galaxies favour the presence of massive dark halos (e.g. Awaki et al. 1994; Loewenstein & White 1999; Mathews & Brighenti 2003; Humphrey et al. 2006). For some controversial galaxies, dark matter appears dynamically absent, perhaps more diffuse than in standard cosmogonies, or possibly disguised by stellar orbital anisotropies (e.g. Méndez et al. 2001; Romanowsky et al. 2003; Dekel et al. 2005; de Lorenzi et al. 2009). In other cases the inference of dark matter is clearer (e.g. O’Sullivan & Ponman 2004; de Lorenzi et al. 2008).

<sup>\*</sup> E-mail: cjs2@mssl.ucl.ac.uk

Gravitational lens models suggest steep, isothermal slopes around the observed radii. However, inner regions show moderate dark matter densities (e.g. Gerhard et al. 2001; Ferreras et al. 2005; Cappellari et al. 2006; Thomas et al. 2007; Weijmans et al. 2009), despite the cuspy predictions of simple collisionless dark matter cosmogonies, and the expectation of adiabatic contraction due to the infall of the baryons towards the centre of the halo (e.g. Blumenthal et al. 1986).

Before N-body simulations became popular and highly resolved, flat-cored profiles like the “pseudo-isothermal sphere” were by default assumed in studies of galaxies and galaxy clusters. Observations of galaxy-scale dark cores now motivate the examination of alternative dark matter theories where the physics naturally cause cores, regardless of any baryonic “feedback” (e.g. Spergel & Steinhardt 2000; Peebles 2000; Arbey et al. 2003; Ahn & Shapiro 2005; Saxton & Wu 2008). Nunez et al. (2006) and Zavala et al. (2006) compared the scaling relations of disc galaxies using either a standard dark matter profile (NFW, Navarro et al. 1996), or a polytrope – intended to represent collisionless dark matter subject to Tsallis thermostats (Tsallis 1988) – and found the latter to explain better the observations. Böhmer & Harko (2007) also found good fits to the rotation curves of low surface brightness galaxies and dwarf galaxies with a polytropic dark matter halo (which they justify via the formation of a Bose-Einstein condensate).

Furthermore, polytropic dark matter halos can equally represent other interesting scenarios, such as self-interacting dark matter, where the core has formed due to the support of dark pressure in the dark field domain. Polytropic models are naturally consistent, self-gravitating distributions of classical mass, and may be seen as analogues to adiabatic fluids. Some early simulations with numerical approximations to dark hydrodynamics (Moore et al. 2000; Yoshida et al. 2000; Burkert 2000; Kochanek & White 2000) entailed (dark) thermal conduction leading to gravothermal catastrophe, and hence isothermal cusps that were sharper than those of collisionless simulations. However it was eventually shown (Balberg & Shapiro 2002; Balberg et al. 2002; Ahn & Shapiro 2005) that the simulations were unwittingly (and inappropriately) initiated in near-collapse conditions. It was shown that conductivity is only significant for SIDM of medium interactivity. Weaker SIDM has infrequent collisions and conduction is slow. Strongly self-interactive dark matter has vanishing conductivity (as it returns to an adiabatic limit) which defers collapse well beyond the age of the universe.

In this paper we extend the polytropic dark halo model of Saxton & Wu (2008) to galaxy scales. We apply the model to fitting planetary nebula and stellar kinematics of elliptical galaxies. We present fits for a number of cases, including “stars only” models, “stars + halo” models with isotropic orbits and a constant global baryon fraction, and finally we also consider the issue of orbital anisotropy and a non-universal baryon fraction.

## 2 METHOD

### 2.1 Spherical model and its solutions

We assume a fixed stellar mass distribution, with a projected surface density approximately described by the Sérsic (1968) profile. Sérsic-like profiles appear ubiquitous among observed galaxy spheroids, although the reasons why this form emerges in nature have not yet been demonstrated analytically. For the three-dimensional stellar density, we adopt the Prugniel & Simien (1997) spherical deprojection (see also Lima Neto et al. 1999; Ciotti & Bertin 1999; Márquez et al. 2000).

$$\rho_{\star}(x) = \rho_e x^{-p} \exp \left[ -b \left( x^{1/n} - 1 \right) \right], \quad (1)$$

with dimensionless coordinate  $x \equiv r/r_e$ , and  $(b, p)$  are constants depending on the index  $n$ . The scale radius (3D) is approximately equal to the observational, projected (2D) half-light radius,  $r_e \approx R_e$ . The stellar mass within some radius is given by

$$m_{\star}(< x) = 4\pi n b^{n(p-3)} e^b \rho_e r_e^3 \Gamma[n(3-p), bx^{1/n}] \quad (2)$$

involving lower incomplete gamma functions.

Within this empirical stellar distribution, we introduce a dark matter halo, with a density distribution to be solved consistently with the global gravitational potential. The local equation of state is polytropic,

$$P_d = s_d \rho_d^{\gamma_d} \quad (3)$$

with a pressure  $P_d$ , density  $\rho_d$ , pseudo-entropy  $s_d$  and adiabatic index  $\gamma_d \equiv 1 + 2/F_d$ . This is the natural behaviour expected for an isotropic medium comprising classical particles with  $F_d$  effective degrees of freedom. Such a condition is expected if dark matter is self-interacting (e.g. Spergel & Steinhardt 2000; Peebles 2000; Arbey et al. 2003; Ahn & Shapiro 2005; Saxton & Wu 2008). An equivalent polytropic equation emerges if the dark halo is governed by Tsallis’ non-extensive thermostats (e.g. Tsallis 1988; Plastino & Plastino 1993; Zavala et al. 2006; Nunez et al. 2006).

If  $-2 < F_d \leq 10$  then the dark halo may truncate at finite mass and radius ( $R_h$ ). For any particular model, we find this radius by assuming dark hydrostasis

$$\frac{dP_d}{dr} = -\frac{Gm\rho_d}{r^2}, \quad (4)$$

where we define the interior mass  $m = m_{\star}(r) + m_d(r)$  for brevity. Computationally, it is more convenient to deal with the dark velocity dispersion (or temperature)  $\sigma_d^2 = P_d/\rho_d$ , which obeys

$$\frac{d\sigma_d^2}{dr} = -\left(\frac{2}{F_d + 2}\right) \frac{Gm}{r^2}. \quad (5)$$

We take  $s_d$  as global constant, and numerically integrate the dark profile from the origin outwards. We assume non-singular conditions at the origin,

$$\left. \frac{d\rho_d}{dr} \right|_{r \rightarrow 0} = 0, \quad (6)$$

precluding the complication of a compact central mass and its sphere of influence. At some point the dark velocity dispersion becomes small (also  $\rho_d \rightarrow 0$  if  $F_d > 0$ ) and the integrator switches to use  $\sigma_d^2$  as the independent variable instead

of  $r$ . Integration proceeds exactly to the point where  $\sigma_d^2 = 0$ , i.e. the natural truncation radius  $R_h$ . We call this the “dark surface”. The low-mass region between the dark core (say where the log-slope of density is  $-2$ ) and the dark surface shall be called the “halo fringe.”

Once the total dark mass  $M_d$  and  $R_h$  are known, we can obtain the external gravitational potential, stellar pressure, potential energy and thermal energy profiles by integrating a Jeans equation (and associated ODEs for the mass profile and potential) inwards from infinity. If we define a stellar pressure in terms of the radial velocity dispersion of stars,  $P_\star \equiv \rho_\star \sigma_\star^2$  then we have the spherical Jeans equation

$$\frac{dP_\star}{dr} = -\frac{Gm\rho_\star}{r^2} - \frac{2\beta P_\star}{r} \quad (7)$$

where  $\beta \equiv 1 - \sigma_\theta^2/\sigma_\star^2$  is the local stellar velocity anisotropy. When integrating (7) far outside the dark halo, we change the independent variable to  $u \equiv 1/r$ . Having obtained all the relevant constants of integration at the dark surface  $R_h$ , we can easily evaluate profiles of the stellar and dark components in both the interior and exterior.

## 2.2 Model specification and projection

In any theory with  $F_d$  dark matter degrees of freedom fixed, the pseudo-entropy  $s_d$  and central dark temperature are formally free parameters. When discussing or fitting families of physically related models, it is more useful to prescribe the stellar mass fraction within some radius,  $\mu_\star(r) = m_\star/(m_\star + m_d)$ , or the dark fraction  $\mu_d = 1 - \mu_\star$ . If galaxies retain all their primordial endowments of matter and darkness, then total stellar value would approximate the cosmic baryon fraction  $\mu_\star(\infty) \approx 0.16^1$ . When seeking particular numerical solutions, we shall attain a chosen  $\mu_\star(\infty)$  by fixing the dark entropy  $s_d$  and adjusting the central  $\sigma_d^2$  iteratively. Then (for a given stellar background) there is an implicit relation between  $s_d$  and the dark truncation radius  $R_h$ .

Model observables are calculated by integrating suitable 3D stellar properties at radii  $r = \sqrt{z^2 + b^2}$  where  $b$  is the projected radius on the sky plane and  $z$  is the line-of-sight coordinate. The column density of stars is simply

$$\Sigma_\star = 2 \int_0^\infty \rho_\star dz, \quad (8)$$

and the sightline integrated pressure is

$$\Pi_\star = 2 \int_0^\infty P_\star \left[ (1 - \beta) + \beta \frac{z^2}{r^2} \right] dz. \quad (9)$$

The mean line-of-sight velocity dispersion is then  $\sigma_{\text{los}} = \sqrt{\Pi_\star/\Sigma_\star}$ . The orbital anisotropy is crucial to the stellar observables. We will mainly consider models with perfect isotropy ( $\beta = 0$  everywhere). In later sections (§3.5), we will consider anisotropy varying radially according to the Osipkov–Merritt model (Osipkov 1979; Merritt 1985),

$$\beta(r) = \frac{r^2}{r^2 + a^2} \quad (10)$$

<sup>1</sup> We note that the latest WMAP-5 results give a best fit for a cosmological baryon fraction of  $\sim 0.2$  (Dunkley et al. 2009). We refer the reader to §3.4 for an estimate of a change in this number.

with the scale radius  $a$  treated as a fitting parameter.

In practice, integration of the stellar profile to radii at large orders of magnitude eventually samples a tenuous, hot region where  $\rho_\star$  drops much faster than  $P_\star$ . Formally, the integrated velocity dispersion rises greatly. Physically, this contribution should not occur, because the densities imply fewer than one star within the relevant volume. Therefore we cut off the integrals (8) and (9) at some three-dimensional radius far outside the kinematic tracers of a particular galaxy.

Calculations are performed in natural units of the Sérsic profile:  $\rho_e = R_e = G = 1$ . A numerical minimal- $\chi^2$  fitting procedure automatically yields the normalisation for a particular data set. This auto-normalisation counts as an extra free parameter, decrementing the “degrees of freedom” in the reduced  $\chi^2$  scores.

## 3 RESULTS

We fit the kinematics of stars and planetary nebulae of a sample comprising twelve galaxies from Coccato et al. (2009) as well as NGC 1400 and NGC 1407. These data are separated into major and minor axis components. We fit the axes separately, to obtain an indication of the applicability of our model’s spherical assumption. Additionally, we fit kinematic data for two of the galaxies without decomposition along axes: for NGC 821 we extract data from Romanowsky et al. (2003). For NGC 3379 we use figure 11 from Douglas et al. (2007). The data for NGC 1400 and 1407 are taken from Proctor et al. (2009). Notice in this case the data are extracted over a circular aperture, so only one axis can be considered.

We assume that the stellar mass component follows the profile of Prugniel & Simien (1997), with the Sérsic parameters shown in the left three columns of Table 1. For nine of the galaxies, these parameters come from photometric fits to Sérsic-only models by Coccato et al. (2009, their table 3). For NGC 3379 we take  $n = 4.7$  from Douglas et al. (2007). For NGC 5128 we assume  $n = 4$  and obtain  $R_e$  from the B-band photometric fit of Dufour et al. (1979). For NGC 5846, we convert Sérsic parameters from Mahdavi et al. (2005). For all galaxies, we keep the distances and luminosities tabulated by Coccato et al. (2009). Initially we attempt fits without a polytrope (“stars only”) to test the necessity of dark matter, and to provide benchmarks for the fitting qualities of halo models.

### 3.1 Fits with stars only

Previous modeling of PN kinematics have suggested a poverty of dark matter in the halos of some isolated elliptical galaxies (Méndez et al. 2001; Romanowsky et al. 2003) or that the halos are less concentrated than popular collisionless dark matter cosmogonies predict (e.g. Douglas et al. 2007; Napolitano et al. 2009; Coccato et al. 2009). To provide baselines for comparison, we first fit the Coccato et al. data with a purely Sérsic model (using the published, photometrically obtained parameters) and no dark matter. Except for NGC 4697, the goodness of fit scores – given by the reduced  $\chi_r^2 \equiv \chi^2/\nu$  – are well above one, and therefore bad fits (see columns 4 and 5 of Table 1 and the solid lines in

figure 1). The model profiles of the projected velocity dispersion are smoothly declining outside a half-light radius, whereas the observational profiles may be flat, or they may dip and rise with radius (Figure 1). Some of these complexities and departures from ideal Sérsic mass profiles may be responsible for the formally poor fits.

### 3.1.1 Improved stellar fits

Using the photometric Sérsic parameters tabulated by Coccato et al. (2009), some galaxies give much worse values for the reduced  $\chi^2$  than others. In order to improve these cases, we try fitting isotropic Sérsic models without dark matter, and adapt the parameters ( $n, R_e$ ) for a better kinematic fit, ( $n', R'_e$ ). In this search, we omit the planetary nebulae, relying on absorption line kinematics only.

Table 1 gives the alternative fits for axes 1 and 2 of each galaxy, before and after kinematic fitting. The left columns are based on Coccato et al. (2009) photometric parameters; the right columns (primed quantities) are our kinematic fits. We give the quality of fit ( $\chi^2_{r'}\}_{1,2}$ ) and the total (stellar) mass  $m_{\star\{1,2\}}$ , where the subindex refers to the axis considered in the analysis. These fits are shown in figure 1 as dotted lines. In some cases we use subindex 0 to refer to data that were obtained within circular annuli. We use an “amoeba” algorithm to find better fitting parameters, ( $n', R'_e$ ), with considerably improved ( $\chi^2_{r'}$ ) on each axis. For NGC 3377, 1407 and 5128 the amoeba runs away forever along a degenerate  $\chi^2$  valley, heading towards  $R_e \rightarrow \infty$ .

In the majority of attempts at ( $n', R'_e$ ) kinematic fits, we find  $R_e$  drifting to large values beyond the data, resulting in unphysically large total stellar masses. NGC 4564 and 3608 have smaller  $R'_e$  than the photometric values. NGC 1023 is the only galaxy where the photometric and kinematic fitted  $R_e$  values are moderate and comparable. Disagreements of photometric and kinematic Sérsic parameters might indicate spatially varying stellar mass/light ratio, or the existence of dark matter. Alternatively, the disagreements may be influenced by degeneracies between the parameters, and the incomplete, finite radial range of the data.

## 3.2 Fitted halos with isotropic orbits

For the Coccato et al. (2009) galaxies, data are available along two principal axes. We fit these independently, using a stellar mass profile with Sérsic model parameters adopted from the published stellar photometry (i.e.  $n$  and  $R_e$  from table 1). The central properties are tuned so that the dark halo and stars are globally in a chosen ratio. We explore cases with fixed  $F_d$ , and vary the halo radius (via  $s_d$ ) to achieve the best fit. Comparing the fits for the two axes gives some indication of the quality of the spherical approximation. (It is an imprecise comparison however, since the minor axis data tend to span a shorter radial range, and are less restrictive.) For six galaxies there are formally satisfactory fits, with  $\chi^2_r \lesssim 1$  (i.e. in NGC 1407, 4374, 4564, 4697, 5128 and 5846). For the rest, the minimal  $\chi^2$  never drops below a few (formally unfavourable). This may be partly due to ideosyncratic stellar kinematic substructures or noisiness.

To address this possibility, we repeat the kinematic fitting process with the stellar  $\sigma_{\text{los}}(r)$  profile smoothed to a

best-fit cubic function in  $\ln(r)$ . PN data are left untouched. Smoothing the stellar kinematics does not shift the minima significantly, but lowers the attainable  $\chi^2$ . Thus the minima are sharper and deeper, but the landscape is unchanged at medium and high  $\chi^2$  levels. Results for the smoothed fitting are shown in Figures 2 and 3. The colours from violet to red represent dark degrees of freedom  $F_d = \{1, 2, 3, \dots, 7, 8, 9, 9.5, 9.9\}$ . The PN velocities were assumed to be isotropic. We assume a universal cosmic fraction of dark and baryonic mass (i.e. stars for our galaxies) according to the WMAP5 cosmology (Dunkley et al. 2009). In figure 3 we show four galaxies for which we have data within circular apertures (Romanowsky et al. 2003; Douglas et al. 2007; Proctor et al. 2009).

The usual  $\chi^2$  curve of a galaxy has two minima: a shallow dip around  $R_h \sim 0.1R_e$  to  $1R_e$ , and a deeper dip at radii outside the observations. The physical interpretation of the inner dip implies a dark halo more compact than the stellar distribution. This would be surprising in the conventional cosmogonies in which radiative cooling made the star-forming gas more concentrated than the dark component. Numerically, at inner-dip configurations the “halo” is taking over the role of the stars influencing the inner  $\sigma_{\text{los}}$  profile. The outer minima seem more physically plausible. Sometimes the outer dip is effectively a lower limit on  $R_h$  (e.g. for NGC 4494) but in other cases the fitting prefers a finite range (e.g. less than  $100R_e$  for NGC 821). If the data are clear and widespread enough, the radial variation of the slope of  $\rho_d$  in the observed range is sufficient to distinguish  $F_d$  and extrapolate the truncation radius. For  $F_d < 9$  the  $\chi^2(R_h)$  curves tend towards the “stars only” level as  $R_h \rightarrow \infty$ . A large- $R_h$  halo (of fixed  $\mu_d$ ) is spread thinly and has negligible effect on observable kinematics. The convergence is closer for lower  $F_d$ , as these models resemble the incompressible limit ( $F_d = 0$ ) which has uniform density within  $r < R_h$ . The highly compressible  $F_d \gtrsim 9$  cases behave quite differently, as discussed in §3.3.

Figure 4 shows the two-dimensional 90, 95 and 99% confidence levels for six galaxies in our sample, in the parameter space spanned by the dark matter degrees of freedom ( $F_d$ ) and the halo truncation radius ( $R_h$ ). The crosses mark the best fit, and the arrow represents the region over which the velocity dispersions are fit. The above mentioned degeneracy seen in the 1D plots of figure 2 is actually a continuous one between  $F_d$  and  $R_h$ .

For three exceptional galaxies (NGC 1023, 3608, 4564) the inner minimum is very significant, or even dominant, in terms of  $\chi^2$ . Inspection of the  $\sigma_{\text{los}}$  profiles shows that the photometrically-derived Sérsic model fits them especially poorly. The inner part of the stellar profile is unusually centrally peaked. NGC 3377 also has a peculiarly shaped  $\sigma_{\text{los}}$  profile, which may be responsible for the slight preference for  $F_d = 9.9$  on the first axis, and for the failure to improve on the stellar-only baseline fit to the second axis. The modelling of these four misfit galaxies implies very small stellar mass to light ratios (in the  $B$ -band), typically  $\Upsilon_{\star}^B \lesssim 0.1\Upsilon_{\odot}^B$  (see NGC 1023<sub>(1,2)</sub>, NGC 3377<sub>(1)</sub> and NGC 4564<sub>(1,2)</sub> in Table 2). This is implausible for the aged stellar populations of early-type galaxies. We deprecate the discussion of these particular galaxies.

Except for these odd cases, the “stars + halo” fits tend to reject  $F_d \gtrsim 9$ . Where the data are clear and smooth



enough, the isotropic modelling generally prefers the dark halo to have  $F_d = 8$  or fewer effective thermal degrees of freedom. There is a mild preference for the top end of the range. In models with  $F_d \geq 9$  the central dark density is insensitive to variations of the outer halo radius ( $R_h$ ) or the halo specific entropy ( $s_d$ ). This inflexibility in fitting central conditions may cause the poor fits for  $F_d \geq 9$ . The best fits favour halo radii of at least tens of  $R_e$ .

We now comment on the favoured isotropic models for specific galaxies.

### 3.2.1 NGC 821

The kinematics of planetary nebulae around NGC 821 show a radially declining velocity dispersion (Romanowsky et al. 2003). This has been taken as evidence disfavouring the presence of a dark halo (unless the PN orbital anisotropy has significant radial variations) or else the halo is less concentrated than CDM expectations.

On both axes of the Coccato et al. (2009) data, we find that polytropic halo models fit significantly better than stars alone. The improvement is best on the first axis. The best fits ( $\chi_r^2 \approx 1.7$ ) are for  $F_d \approx 8$  and an outer radius  $60 \lesssim R_h/R_e \lesssim 90$ . These minima improve significantly upon the “stars only” fit, in the case of axis 1 by up to  $\Delta\chi_r^2 \sim 25$ .

The upper left panel of Figure 3 presents the equivalent reduced- $\chi^2$  scores obtained by fitting polytropic dark halos to the Romanowsky et al. (2003) data for NGC 821. These data were annular in distribution (not divided onto axes) and less detailed than Coccato et al. (2009). The fits also prefer  $F_d \approx 8$ , but the minima are shallower. For  $F_d = 8$  the fit improves gradually for larger  $R_h$ , but for  $F_d \leq 7$  there is an optimum at several tens of  $R_e$ . For the dark mass fraction within  $1R_e$ , the most likely value is  $\approx 0.2 - 0.4$ , comparable to the Coccato et al. (2009) value ( $\approx 0.4$ ). The best fit stellar mass-to-light ratio  $\Upsilon_\star^B \sim 5\Upsilon_\odot^B$  is typical of metal-rich populations of age 5-6 Gyr (see e.g. Bruzual & Charlot 2003).

### 3.2.2 NGC 1023

Our analysis favours a dark halo with  $F_d \approx 9.9$  (near maximum) and small radius  $R_h < 10R_e$ . The poor halo fits for this galaxy are perhaps unsurprising given the poor fits to the “stars only” basic model. The stellar  $\sigma_{\text{los}}$  profile is more centrally peaked than the (photometric) Sérsic model. It was observed (Noordermeer et al. 2008; Coccato et al. 2009) that the inner regions ( $r < 100''$ ) are affected by strong rotation. NGC 1023 is a SB0 galaxy with a fast rotating bar which would imply a maximal (i.e. baryon dominated) disc (Debattista et al. 2002). We omit NGC 1023 in the analysis.

### 3.2.3 NGC 1344

Fits to data from axis 2 are bad mainly because of the flat plateau in velocity dispersion in the inner region. Axis 1 gives an acceptable fit for  $F_d \sim 6$ , with a significant improvement over the stars-only model. According to Teodorescu et al. (2005), there is a  $3.8 \times 10^{11} M_\odot$  dark matter halo out to  $3.5R_e$ . A rough estimate of the baryon fraction – assuming 90% of the stellar mass is contained within  $3.5R_e$

(Graham et al. 2005) – gives a baryon fraction within this region of 0.29, in agreement with our estimates ( $f_B \sim 0.3$ ).

### 3.2.4 NGC 1400

This lenticular galaxy is one of the two bright members of a nearby group (along with NGC 1407, Gould 1993). We extract the stellar kinematics from Proctor et al. (2009). We take their assumed distance, but use the B magnitude and Sérsic model from Spolaor et al. (2008). Assuming a cosmic baryon fraction, none of the polytropic halo models fits as well as “stars only.” Perhaps this is attributable to the discrepancies between  $\sigma_{\text{los}}$  profiles from different observations (noted by Proctor et al. 2009). We also notice that NGC 1400 has a significant amount of rotation ( $v/\sigma \sim 0.5$  at  $R_e$ , Bertin et al. 1994), which could possibly explain its +0.3 dex residual with respect to the Fundamental Plane (Prugniel & Simien 1996).

### 3.2.5 NGC 1407

This E0 galaxy is the brightest member of a nearby group (including NGC 1400, Gould 1993). The stellar data were extracted from Proctor et al. (2009), and we refer again to Spolaor et al. (2008) for the light profile. The polytropic model with cosmic dark matter fraction gives a good fit, with  $F_d \approx 7$  and truncation radius  $\sim 15R_e$ . The halo models with  $F_d \gtrsim 9$  have significantly poorer fits than for low and medium effective degrees of freedom.

### 3.2.6 NGC 3377

Stellar data for this flattened (E5) galaxy show a pronounced “S-bend” in the  $\sigma_{\text{los}}$  profile. All the fits are formally bad. On the first axis, a halo with high  $F_d$  brings a slight – but perhaps insignificant – improvement. On the second axis, a dark halo does not improve the fit at all, and the  $F_d = 9.5$  and 9.9 curves are worse than the others. We suspect that complicated orbital structure (especially the undulating projected kinematics) renders straightforward spherical models inadequate and inapplicable to NGC 3377. Details of this profile have been attributed to the influence of a central massive object and discy dynamics (Gebhardt et al. 2003; Copin et al. 2004). Coccato et al. (2009) note a twist in the PN kinematics. We omit NGC 3377 from consideration in our conclusions.

### 3.2.7 NGC 3379

This galaxy is another of the notable systems that Romanowsky et al. (2003) observed to have a radially declining  $\sigma_{\text{los}}$  profile. For the Coccato et al. (2009) data on two axes, the dark halo does not improve the fits over a Sérsic-only model. Dark matter is allowed if the halo has a large radius and low central concentration. Cases with  $F_d \geq 9$  are much worse fits than for lower  $F_d$ .

For comparison with the split-axial results, we also fit the projected velocity dispersion data representing circular rings, which are extracted from figure 11 of Douglas et al. (2007) (who incorporated stellar data from Statler & Smecker-Hane 1999). A purely stellar model fits

poorly: if the orbits are isotropic then  $\chi_r^2 \approx 4.1$ . If dark matter is present in the cosmic fraction, then it improves the fitting somewhat: the best  $\chi_r^2 \approx 2$  occurs for  $F_d \approx 7$  (see lower middle panel, Figure 2). Isotropic models with  $F_d \geq 9$  fit unacceptably worse than those with  $F_d \leq 8$ .

The simple Sérsic model of the stellar mass may be inadequate to improve upon these fits. A bump in the stellar  $\sigma_{\text{los}}$  profile suggests the presence of kinematic substructure.

### 3.2.8 NGC 3608

Including a dark halo does not improve on stellar-only fits. The minima – which have very high values of  $\chi_r^2$  – either imply a very compact halo ( $R \sim 1R_e$ ) with  $F_d > 9$  or an extended halo ( $\sim 500R_e$ ) with  $F_d = 1$ . We tentatively blame this outcome on the centrally peaky  $\sigma_{\text{los}}$  profile. If the Sérsic profile describes the stellar mass distribution poorly, then the fitting routine compensates by seeking a high central dark density. Coccato et al. (2009) remark that this galaxy had few PN detections, and possible contamination from NGC 3607 nearby. We omit NGC 3608 from further detailed examination.

### 3.2.9 NGC 4374

This E1 radio galaxy (Messier 84) is a member of the Virgo cluster. Fits to this galaxy favour the presence of a dark halo, with  $F_d \approx 8$  and  $R \approx 100$  to  $1000R_e$ . Unusually, for the second axis, the  $F_d = 9$  case improves on the basic “stars only” model (although  $F_d \approx 8$  is still the best fit).

### 3.2.10 NGC 4494

This is another of the intriguing cases where Romanowsky et al. (2003) found a declining velocity profile implying a dark matter halo with a very low density (Napolitano et al. 2009). From data on both axes of Coccato et al. (2009), the fitting characteristics resemble those of NGC 3379: dark matter brings no improvement. A halo is allowed if its outer radius far exceeds the observed region.

### 3.2.11 NGC 4564

Models fitted to this E6 galaxy strongly prefer the presence of dark matter, but with radius of only a few  $R_e$ . Perhaps this surprising conclusion is due to the centrally peaky stellar  $\sigma_{\text{los}}$  profile. The mass and orbital distributions may depart significantly from a Sérsic sphere. Coccato et al. (2009) indicate that there is a rotation curve resembling “an S0 galaxy rather than ... an elliptical galaxy”. The unphysically low values of M/L and of the baryon fraction confirm the fit for this galaxy must invoke non-spherical models. We omit NGC 4564 from the analysis.

### 3.2.12 NGC 4697

This flattened elliptical (E6) galaxy has especially numerous PN measurements. Its velocity dispersion declines in the outskirts, and the degree of rotation appears to decline outside  $R_e$  (Méndez et al. 2001, 2008; Sambhus et al.

2006; de Lorenzi et al. 2008; Coccato et al. 2009). Despite the non-sphericity, our fits to both axes favour the presence of a dark halo with  $F_d \approx 7$  or 8 consistently. The extrapolated outer radius is large,  $R_h \gg 100R_e$ . Thus the characteristics of this galaxy are consistent with the other apparently good fits.

### 3.2.13 NGC 5128

For the famous nearby galaxy NGC 5128 (Centaurus A) the axis 1 data strongly favour the presence of a dark halo with cosmically mean composition. The best fit indicates  $F_d \approx 6$  and  $R \approx 25R_e$ . This is fewer dark thermal degrees of freedom than in our other plausible fits. The halo radius also seems more compact than usual. The prominent dust lane implies a recent merger, which might have left persistent departures from spherical hydrostasis in the dark sector as well. (Persistent dark pulsations or rotation could possibly change the apparent  $F_d$  obtainable from inapplicable static kinematics.) Unfortunately the results from axis 2 are inconclusive due to insufficient data.

### 3.2.14 NGC 5846

NGC 5846 is the central galaxy of a nearby group, and it appears round (morphological type E0-E1) and non-rotating (Coccato et al. 2009). We should have expected decisive fits. The Sérsic parameters are debatable: by fitting stellar and PN photometry, Coccato et al. (2009) find  $n = 12 \pm 2$ ,  $R_e = 2903 \pm 192''$ . However Mahdavi et al. (2005) fit the light profile with  $n = 3.95 \pm 0.05$  and  $R_e = 69.5 \pm 5.5''$ . We adopt the latter parameter pair (high Sérsic indices, normally paired with very large half-light radii are usually indicative of a fitting degeneracy). Our fits to axis 1 marginally favour a dark halo with a small outer radius,  $R_h \approx 7.8R_e$ , and  $F_d \approx 1$ . On axis 2, the Sérsic-only fit is similar to a stellar+dark matter model.

## 3.3 Features of the dark matter profile

In a Lane-Emden sphere unaffected by other mass components, the quasi-entropy can take any positive real value, and there is a one-to-one relation between the entropy and the natural outer truncation radius of the halo. We find that this is untrue for a halo perturbed by a Prugniel & Simien (1997) stellar component. For  $F_d \gtrsim 6$  or so, we numerically find that there is a minimum  $s_d$  at which the halo fringe becomes infinitely diffuse, failing to truncate. For many models the cosmic baryon fraction is unattainable beyond a particular range of the entropy (even if the halo is finite).

The poor fitting by  $F_d \gtrsim 9$  halos has a related cause. When the degrees of freedom are numerous, the core is smaller and denser compared to the outskirts. This dense core tends to outweigh the central stellar density, providing a poor fit to the inner data. For  $F_d \gtrsim 9$  the dark mass always outweighs the stars within  $1R_e$  (see upper lines in figure 5). Furthermore, when  $F_d \geq 9$  we find that inflating the halo (extending the fringe radially) does not reduce the central dark density significantly. For lower  $F_d$ , the core expands somewhat as the truncation radius increases, and

this enables fits with plausibly low dark densities within the half-light radius.

Figure 6 illustrates the halo density profile for the best-fitting models of axis 1 of NGC 821 for the choices of  $F_d$  as shown in figure 2 (with the same colour coding). In our fits, this galaxy possesses a significant dark mass fraction within the half-light radius, and the dark density at  $1R_e$  is comparable to the stellar density there. The  $F_d \geq 9$  curves are structurally distinct: the dark density follows that of the stars closely for several decades in radius. The truncation radius is large, but nevertheless the central dark density is high. The more favourable fits, with  $F_d \leq 8$ , involve halos that truncate within  $100R_e$ , and there is a much larger inner region where  $\rho_d > \rho_\star$  (e.g.  $r \approx 0.7R_e$  for  $F_d = 8$ ). For all fits, the logarithmic slope of the dark matter halo density is around  $-1$  around and within the half-light radius. This should not be mistaken for the  $\rho_d \propto r^{-1}$  cusps of collisionless N-body simulations. The innately flat core of the polytropic halo has been gravitationally pinched by the stellar mass distribution. The *total* mass density index wavers around  $-2$  out to several  $R_e$ , which may be consistent with implications from some gravitational lensing studies (Rusin et al. 2003; Koopmans et al. 2006; Ferreras et al. 2008). If  $F_d < 9$  and if our models have typical mass concentrations then the polytropic halo of a truly isolated elliptical galaxy would eventually be found to decline more sharply than  $\propto r^{-3}$ , somewhere beyond  $\sim 10R_e$ . Satellite galaxies and correlated cosmological macrostructure in the vicinity may confuse the practical detection of this truncation.

Figure 7 shows the scatter of the baryon fraction with respect to stellar masses for the best-fit models that adequately improve over the stellar-only baseline cases. Solid dots represent those galaxies with a good fit ( $\chi_r^2 < 3$ ). The figure shows that within  $1R_e$  most galaxies appear baryon dominated except for massive ones, mainly NGC 1407. At  $5R_e$  the baryon fraction decreases in most cases to  $\sim 20\%$ . For comparison, the analysis of strong gravitational lenses from SLACS (Bolton et al. 2008) is shown as a grey shade in the left panel – the SDSS-selected lenses mainly probe the inner ( $R \lesssim R_e$ ) regions. There is also consistency with the estimates of Cappellari et al. (2006) using the SAURON sample – they quote a dark matter fraction of  $\sim 30\%$  in the inner  $R_e$ ; or with the recent work of Tortora et al. (2009), with similar values. The grey cross and error bars in figure 7 (*right*) correspond to the lensing analysis of the galaxy B1104-181 (at a redshift  $z=0.73$ ) from Ferreras et al. (2005), which was observed within  $R < 3.7R_e$  (limited by the position of the lensed images of the background source, which controls the accuracy of the lensing estimates).

### 3.4 Stellar brightness and mass fraction

Though we have only fourteen galaxies (and not all of them with satisfactory fits) it is interesting to consider their apparent properties as a population. Figure 8 shows the relation between *B*-band stellar mass-to-light ratio ( $\Upsilon_\star$ ) and the total stellar masses ( $m_\star$ ), which are obtained jointly from the fitting process. Those galaxies with a good fit ( $\chi_r^2 < 3$ ) are shown as solid dots. In grey we also show the *dynamical* M/L values from van der Marel & van Dokkum (2007) for the galaxies in our sample. Those values are typically obtained within  $R_e$ , and agree rather well with our

estimates using a polytropic dark matter halo. For comparison with stellar populations, we also show in the right side of figure 8 the expected stellar M/L for a couple of synthetic stellar populations from the CB07 models (e.g. Bruzual A 2007) for a Chabrier (2003) IMF. Two metallicities are considered, as labelled. We find that the more massive galaxies tend to have older stellar populations with ages compatible with more detailed work based on equivalent widths (see e.g. Thomas et al. 2005; Rogers et al. 2009).

Among our standard calculations, NGC 821 shows perhaps the most convincing evidence for a dark halo of cosmic mass fraction. In a set of exploratory calculations, we vary the assumed ratio of stellar to dark mass for this particular galaxy. As illustrated in Figure 9, the stellar mass fraction  $\mu_\star(\infty)$  does have some effect. If the galaxy is richer in dark matter than the cosmic mean, then the best model shifts towards slightly higher  $F_d$ , e.g. for  $\mu_\star = 0.05$  – a value motivated by the latest estimates of the baryon fraction in galaxy halos (see e.g. Moster et al. 2009; Guo et al. 2009) – the optimum is around  $F_d \approx 9$  with  $R_h \approx 457R_e$ . If the galaxy is poor in dark matter then  $F_d$  and  $R_h$  both shift to lower values. As  $\mu_\star \rightarrow 1$ , the  $\chi^2$  curves collapse trivially to the poor fit of the “stars only” model. The best  $\chi^2$  indicates moderate depletion of dark matter, e.g. when fixing  $\mu_\star = 0.30$  we find  $\chi_r^2 = 0.98$  and  $R_h \approx 4.94R_e$  for  $F_d = 3$ . This would imply halo truncation within the span of the observed planetary nebulae. Models with  $\mu_\star(\infty) \lesssim 0.2$  do not imply such a peculiarity.

### 3.5 Effect of radial orbital anisotropy

To explore the role of orbital anisotropy, we try re-fitting some of the galaxies assuming the Osipkov-Merritt profile for  $\beta(r)$  (see equation 10). In this model, stellar orbits are isotropic in the centre, and increasingly radial in the fringe beyond a scale radius  $a$  (Osipkov 1979; Merritt 1985). For “stars only” fits the OM radial anisotropy profile provides negligible improvement if the scale radius  $a$  is large (approaching isotropic models), and for small  $a$  it makes the  $\chi^2$  scores significantly worse. Therefore radial anisotropy in the outskirts seems unlikely to cure the apparent dark deficit (or low halo concentration) of cases like NGC 4494. In this sense, “stars alone” models may be insufficient without non-spherical effects.

Figure 10 shows the effect of Osipkov-Merritt radial orbital anisotropy profiles upon “stars + halo” models of NGC 821 (axis 1). NGC 821 is one of the cases with a clear need for a dark halo and this persists when the fringe is radially anisotropic. The  $\chi^2$  curves still discriminate between  $F_d$  sharply. The curves prefer low  $F_d$  if  $a < 2$ ; for  $a = 2$  the optimum is  $F_d = 3$ ; for  $a = 3$  it is  $F_d = 6$ . Thus the Osipkov-Merritt radial anisotropy model favours small  $F_d$  if the scale radius is comparable to the half-light radius, while isotropic models favour  $F_d \approx 8$ . The effects of the OM model are similar for other galaxies, such as NGC 3379. Overall  $\chi^2$  levels are lower for larger  $a$ , and thus the isotropic limit is formally favourable. To convincingly constrain the amount and functional form of the anisotropy profile, it would be necessary to fit more detailed models with axisymmetry or fitting velocity kurtosis data. Such complexity is beyond the scope of our present paper.

### 3.6 Exotic models: $-2 < F_d < 0$

It is worth mentioning the mathematical existence of a range of more exotic polytropes, with negative degrees of freedom. Models with  $-2 < F_d < 0$  and negative pressure ( $P_d < 0$ ,  $s_d < 0$ ) describe a “generalised Chaplygin gas,” which has been proposed to unify dark matter and dark energy (e.g. Bento et al. 2002; Bilic et al. 2002; Bertolami et al. 2004). Polytropes with this composition have infinite radius and mass, so they need arbitrary truncation at some background density (e.g. Bertolami & Páramos 2005). Thus it is unclear how to naturally constrain the dark mass fraction in Chaplygin models of galaxies.

However, if the pressure is positive, then the mass and radius of the halo are finite (Viala & Horedt 1974a,b; Kimura 1981; Lipscombe 2008). In this “anti-Chaplygin gas” halo, density is minimal at the origin, and increases to infinity at the outer radius  $R_h$  where temperature drops to zero. (Farther out, the dark density stays zero, as it does outside normal polytropes with  $0 < F_d < 10$ .) These peculiar bubble-halo models are calculable, though the infinitely dense surface causes difficulty for the numerical integrators that project  $\sigma_{\text{los}}$ . We performed a sparse set of exploratory calculations in this regime, and find a continuation of the trends in  $\chi^2(R_h, F_d)$  already seen at the low end of the  $F_d > 0$  domain. For NGC 821, the  $\chi^2$  optimum rises (poorer fitting) and continues smoothly shifting to smaller  $R_h$  as  $F_d \searrow -2$ .

The limit of  $F_d = -2$  describes an isobaric condition. In this case, hydrostasis requires the gravitational field to vanish everywhere. There are no bound, finite, static, spherical, adiabatic solutions. The choice of  $F = -2$  and  $P_d = 0$  could describe a collisionless medium, but the dark density and entropy  $s_d$  would then be arbitrarily spatially variable (which is a complication beyond the scope of this paper).

## 4 CONCLUSIONS

We have fitted published kinematics of fourteen diverse elliptical galaxies, assuming a Sérsic stellar mass profile plus a spherical polytropic dark matter halo that is distributed self-consistently in the shared gravitational field. This non-standard model is justified by our current lack of knowledge about the nature of the dark matter particle. A non-zero cross section for non-gravitational interactions or internal degrees of freedom will justify this interpretation. Furthermore, studies on the effect of gravitation on an ensemble of particles suggest a polytropic equation of state is required even if we are dealing with a non-interacting, elementary particle (Tsallis 1988).

Our fits imply that more massive galaxies have higher stellar mass-to-light ratios, and higher central fractions of dark matter. We also impose a constraint on the degrees of freedom for the dark matter particle,  $F_d \gtrsim 6$ , in agreement with a previous study focussed on galaxy clusters (Saxton & Wu 2008). The favoured  $F_d$  increases to higher values if elliptical galaxies are poorer in dark matter (and the favoured  $F_d$  is smaller if baryons are lost). Dark matter fractions well above or below the cosmic fractions may be explicable in several ways. Dark matter may be lost via ablation or tidal stripping, especially in dense environments.

Baryonic matter might be lost due to blowout from stellar or AGN feedback, or from inefficient cooling (at the massive end), letting the baryons escape as warm or hot IGM/ICM unbound to the galaxy.

The tentative preference for six to eight dark matter thermal degrees of freedom is interesting when compared to circumstantial evidence from galaxy clusters. In their analyses of galaxy clusters comprising polytropic dark matter and radiative gas, Saxton & Wu (2008) found that the condition for stationary solutions implies a lower limit on the central mass. Compatibility with the scale of observed supermassive black holes (as well as the dark matter core radii of clusters) implies a constraint of  $7 \lesssim F_d \lesssim 10$ . (The upper limit is necessary to form any finite self-gravitating body.) Taken together, the evidence from elliptical galaxies and galaxy clusters therefore implies that dark matter has  $F_d \sim 7$  to 8 (if it is the same substance in both contexts).

Half of the available galaxies are well fit by the polytropic halo model, despite its serious physical simplifications. Some galaxies may require tailored, non-spherical modelling or special treatment of the kinematic relics of their idiosyncratic merger histories. We have assumed that the adiabatic dark halo is well mixed and is non-rotating; this may be untrue for a galaxy that has merged less than a few dynamical times ago. Our present modelling precludes the possible effects of a central star cluster or giant black hole, either of which could induce a parsec-scale spike of dark and stellar matter (within some gravitational radius of influence). This could raise the central velocity dispersion. Allowing this feature to emerge in future models might improve fits to the three galaxies with centrally spiky  $\sigma_{\text{los}}(r)$  profiles.

## ACKNOWLEDGMENTS

We thank: K. Wu for encouragement and criticism. M. Cappellari for a conversation prompting this work. N. Napolitano and L. Coccato for their provision of online data.

## REFERENCES

- Ahn K., Shapiro P. R., 2005, MNRAS, 363, 1092
- Arbey A., Lesgourgues J., Salati P., 2003, Phys. Rev. D, 68, 023511
- Awaki H., Mushotzky R., Tsuru T., Fabian A. C., Fukazawa Y., Loewenstein M., Makishima K., Matsumoto H., Matsushita K., Mihara T., Ohashi T., Ricker G. R., Serlemitsos P. J., Tsusaka Y., Yamazaki T., 1994, PASJ, 46, L65
- Balberg S., Shapiro S. L., 2002, Physical Review Letters, 88, 101301
- Balberg S., Shapiro S. L., Inagaki S., 2002, ApJ, 568, 475
- Bento M. C., Bertolami O., Sen A. A., 2002, Phys. Rev. D, 66, 043507
- Bertin G., Bertola F., Buson L. M., Danzinger I. J., Dejonghe H., Sadler E. M., Saglia R. P., de Zeeuw P. T., Zeilinger W. W., 1994, A&A, 292, 381
- Bertolami O., Páramos J., 2005, Phys. Rev. D, 72, 123512
- Bertolami O., Sen A. A., Sen S., Silva P. T., 2004, MNRAS, 353, 329



- Bilic N., Munyaneza F., Tupper G. B., Viollier R. D., 2002, *Progress in Particle and Nuclear Physics*, 48, 291
- Binney J., Mamon G. A., 1982, *MNRAS*, 200, 361
- Blumenthal G. R., Faber S. M., Flores R., Primack J. R., 1986, *ApJ*, 301, 27
- Böhmer C. G., Harko T., 2007, *Journal of Cosmology and Astro-Particle Physics*, 6, 25
- Bolton A. S., Treu T., Koopmans L. V. E., Gavazzi R., Moustakas L. A., Burles S., Schlegel D. J., Wayth R., 2008, *ApJ*, 684, 248
- Bruzual G., Charlot S., 2003, *MNRAS*, 344, 1000
- Bruzual A G., 2007, *ArXiv Astrophysics e-prints*, astro-ph/0703052
- Burkert A., 1995, *ApJ*, 447, L25
- Burkert A., 2000, *ApJ*, 534, L143
- Cappellari M., Bacon R., Bureau M., Damen M. C., Davies R. L., de Zeeuw P. T., Emsellem E., Falcón-Barroso J., Krajnović D., Kuntschner H., McDermid R. M., Peletier R. F., Sarzi M., van den Bosch R. C. E., van de Ven G., 2006, *MNRAS*, 366, 1126
- Chabrier G., 2003, *PASP*, 115, 763
- Ciotti L., Bertin G., 1999, *A&A*, 352, 447
- Coccato L., Gerhard O., Arnaboldi M., Das P., Douglas N. G., Kuijken K., Merrifield M. R., Napolitano N. R., Noordermeer E., Romanowsky A. J., Capaccioli M., Cortesi A., de Lorenzi F., Freeman K. C., 2009, *MNRAS*, 394, 1249
- Copin Y., Cretton N., Emsellem E., 2004, *A&A*, 415, 889
- de Blok W. J. G., 2005, *ApJ*, 634, 227
- de Lorenzi F., Gerhard O., Coccato L., Arnaboldi M., Capaccioli M., Douglas N. G., Freeman K. C., Kuijken K., Merrifield M. R., Napolitano N. R., Noordermeer E., Romanowsky A. J., Debattista V. P., 2009, *MNRAS*, 395, 76
- de Lorenzi F., Gerhard O., Saglia R. P., Sambhus N., Debattista V. P., Pannella M., Méndez R. H., 2008, *MNRAS*, 385, 1729
- Debattista V. P., Corsini E. M., Aguerri J. A. L., 2002, *MNRAS*, 332, 65
- Dekel A., Stoehr F., Mamon G. A., Cox T. J., Novak G. S., Primack J. R., 2005, *Nature*, 437, 707
- Diemand J., Moore B., Stadel J., 2004, *MNRAS*, 353, 624
- Diemand J., Zemp M., Moore B., Stadel J., Carollo C. M., 2005, *MNRAS*, 364, 665
- Douglas N. G., Napolitano N. R., Romanowsky A. J., Coccato L., Kuijken K., Merrifield M. R., Arnaboldi M., Gerhard O., Freeman K. C., Merrett H. R., Noordermeer E., Capaccioli M., 2007, *ApJ*, 664, 257
- Dubinski J., Carlberg R. G., 1991, *ApJ*, 378, 496
- Dufour R. J., Harvel C. A., Martins D. M., Schiffer III F. H., Talent D. L., Wells D. C., van den Bergh S., Talbot Jr. R. J., 1979, *AJ*, 84, 284
- Dunkley J., Komatsu E., Nolte M. R., Spergel D. N., Larson D., Hinshaw G., Page L., Bennett C. L., Gold B., Jarosik N., Weiland J. L., Halpern M., Hill R. S., Kogut A., Limon M., Meyer S. S., Tucker G. S., Wollack E., Wright E. L., 2009, *ApJS*, 180, 306
- Ferreras I., Saha P., Williams L. L. R., 2005, *ApJ*, 623, L5
- Ferreras I., Saha P., Williams L. L. R., Burles S., 2008, in J. Davies & M. Disney ed., *IAU Symposium Vol. 244 of IAU Symposium, Mapping the Distribution of Luminous and Dark Matter in Strong Lensing Galaxies*. pp 206–215
- Flores R. A., Primack J. R., 1994, *ApJ*, 427, L1
- Gebhardt K., Richstone D., Tremaine S., Lauer T. R., Bender R., Bower G., Dressler A., Faber S. M., Filippenko A. V., Green R., Grillmair C., Ho L. C., Kormendy J., Magorrian J., Pinkney J., 2003, *ApJ*, 583, 92
- Gentile G., Salucci P., Klein U., Vergani D., Kalberla P., 2004, *MNRAS*, 351, 903
- Gerhard O., Kronawitter A., Saglia R. P., Bender R., 2001, *AJ*, 121, 1936
- Gnedin O. Y., Kravtsov A. V., Klypin A. A., Nagai D., 2004, *ApJ*, 616, 16
- Gnedin O. Y., Zhao H., 2002, *MNRAS*, 333, 299
- Gould A., 1993, *ApJ*, 403, 37
- Graham A. W., Driver S. P., Petrosian V., Conselice C. J., Bershadsky M. A., Crawford S. M., Goto T., 2005, *AJ*, 130, 1535
- Guo Q., White S., Li C., Boylan-Kolchin M., 2009, *ArXiv e-prints*, 0909.4305
- Humphrey P. J., Buote D. A., Gastaldello F., Zappacosta L., Bullock J. S., Brighenti F., Mathews W. G., 2006, *ApJ*, 646, 899
- Jardel J. R., Sellwood J. A., 2009, *ApJ*, 691, 1300
- Kimura H., 1981, *PASJ*, 33, 749
- Kochanek C. S., White M., 2000, *ApJ*, 543, 514
- Koopmans L. V. E., Treu T., Bolton A. S., Burles S., Moustakas L. A., 2006, *ApJ*, 649, 599
- Kuzio de Naray R., McGaugh S. S., de Blok W. J. G., Bosma A., 2006, *ApJS*, 165, 461
- Lima Neto G. B., Gerbal D., Márquez I., 1999, *MNRAS*, 309, 481
- Lipscombe T. C., 2008, *ArXiv e-prints*, 0812.1502
- Loewenstein M., White III R. E., 1999, *ApJ*, 518, 50
- Mahdavi A., Trentham N., Tully R. B., 2005, *AJ*, 130, 1502
- Márquez I., Lima Neto G. B., Capelato H., Durret F., Gerbal D., 2000, *A&A*, 353, 873
- Mathews W. G., Brighenti F., 2003, *ARA&A*, 41, 191
- Méndez R. H., Riffeser A., Kudritzki R.-P., Matthias M., Freeman K. C., Arnaboldi M., Capaccioli M., Gerhard O. E., 2001, *ApJ*, 563, 135
- Méndez R. H., Teodorescu A. M., Kudritzki R.-P., 2008, *ApJS*, 175, 522
- Merritt D., 1985, *MNRAS*, 214, 25P
- Moore B., 1994, *Nature*, 370, 629
- Moore B., Gelato S., Jenkins A., Pearce F. R., Quilis V., 2000, *ApJ*, 535, L21
- Moore B., Governato F., Quinn T., Stadel J., Lake G., 1998, *ApJ*, 499, L5
- Moster B. P., Somerville R. S., Maubetsch C., van den Bosch F. C., Maccio' A. V., Naab T., Oser L., 2009, *ArXiv e-prints*, 0903.4682
- Napolitano N. R., Romanowsky A. J., Coccato L., Capaccioli M., Douglas N. G., Noordermeer E., Gerhard O., Arnaboldi M., de Lorenzi F., Kuijken K., Merrifield M. R., O'Sullivan E., Cortesi A., Das P., Freeman K. C., 2009, *MNRAS*, 393, 329
- Navarro J. F., Frenk C. S., White S. D. M., 1996, *ApJ*, 462, 563
- Noordermeer E., Merrifield M. R., Coccato L., Arnaboldi M., Capaccioli M., Douglas N. G., Freeman K. C., Gerhard O., Kuijken K., de Lorenzi F., Napolitano N. R., Romanowsky A. J., 2008, *MNRAS*, 384, 943
- Nunez D., Sussman R. A., Zavala J., Cabral-Rosetti L. G.,

- Matos T., 2006, in Pérez M. A., Urrutia L., Villaseqor L., eds, *Particles and Fields: X Mexican Workshop Vol. 857* of American Institute of Physics Conference Series, Empirical testing of Tsallis' Thermodynamics as a model for dark matter halos. pp 316–320
- Osipkov L. P., 1979, *Soviet Astronomy Letters*, 5, 42
- O'Sullivan E., Ponman T. J., 2004, *MNRAS*, 354, 935
- Peebles P. J. E., 2000, *ApJ*, 534, L127
- Plastino A. R., Plastino A., 1993, *Physics Letters A*, 174, 384
- Proctor R. N., Forbes D. A., Romanowsky A. J., Brodie J. P., Strader J., Spolaor M., Mendel J. T., Spitler L., 2009, *ArXiv e-prints*, 0905.4424
- Prugniel P., Simien F., 1996, *A&A*, 309, 749
- Prugniel P., Simien F., 1997, *A&A*, 321, 111
- Rogers B., Ferreras I., Peletier R., Silk J., 2009, *MNRAS*, pp 1755–+
- Romano-Díaz E., Shlosman I., Hoffman Y., Heller C., 2008, *ApJ*, 685, L105
- Romanowsky A. J., Douglas N. G., Arnaboldi M., Kuijken K., Merrifield M. R., Napolitano N. R., Capaccioli M., Freeman K. C., 2003, *Science*, 301, 1696
- Rusin D., Kochanek C. S., Falco E. E., Keeton C. R., McLeod B. A., Impey C. D., Lehár J., Muñoz J. A., Peng C. Y., Rix H., 2003, *ApJ*, 587, 143
- Sambhus N., Gerhard O., Méndez R. H., 2006, *AJ*, 131, 837
- Saxton C. J., Wu K., 2008, *MNRAS*, 391, 1403
- Sérsic J. L., 1968, *Atlas de galaxias australes*. Cordoba, Argentina: Observatorio Astronomico, 1968
- Simon J. D., Bolatto A. D., Leroy A., Blitz L., Gates E. L., 2005, *ApJ*, 621, 757
- Spergel D. N., Steinhardt P. J., 2000, *Physical Review Letters*, 84, 3760
- Spolaor M., Forbes D. A., Hau G. K. T., Proctor R. N., Brough S., 2008, *MNRAS*, 385, 667
- Springel V., Frenk C. S., White S. D. M., 2006, *Nature*, 440, 1137
- Statler T. S., Smecker-Hane T., 1999, *AJ*, 117, 839
- Teodorescu A. M., Méndez R. H., Saglia R. P., Riffeser A., Kudritzki R.-P., Gerhard O. E., Kleya J., 2005, *ApJ*, 635, 290
- Thomas D., Maraston C., Bender R., Mendes de Oliveira C., 2005, *ApJ*, 621, 673
- Thomas J., Saglia R. P., Bender R., Thomas D., Gebhardt K., Magorrian J., Corsini E. M., Wegner G., 2007, *MNRAS*, 382, 657
- Tortora C., Napolitano N. R., Romanowsky A. J., Capaccioli M., Covone G., 2009, *MNRAS*, 396, 1132
- Tsallis C., 1988, *Journal of Statistical Physics*, 52, 479
- van der Marel R. P., van Dokkum P. G., 2007, *ApJ*, 668, 756
- Viala Y., Horedt G. P., 1974a, *A&AS*, 16, 173
- Viala Y. P., Horedt G., 1974b, *A&A*, 33, 195
- Weijmans A., Cappellari M., Bacon R., de Zeeuw P. T., Emsellem E., Falcón-Barroso J., Kuntschner H., McDermid R. M., van den Bosch R. C. E., van de Ven G., 2009, *MNRAS*, 398, 561
- Weijmans A.-M., Krajnović D., van de Ven G., Oosterloo T. A., Morganti R., de Zeeuw P. T., 2008, *MNRAS*, 383, 1343
- Weldrake D. T. F., de Blok W. J. G., Walter F., 2003, *MNRAS*, 340, 12
- Yoshida N., Springel V., White S. D. M., Tormen G., 2000, *ApJ*, 544, L87
- Zavala J., Núñez D., Sussman R. A., Cabral-Rosetti L. G., Matos T., 2006, *Journal of Cosmology and Astro-Particle Physics*, 6, 8

**Table 1.** Reduced  $\chi^2$  values for isotropic fits omitting PN data, with a Sérsic (stellar) mass component only. There are too few data on axis 2 of NGC 5128, so in this case we fit both axes together. NGC 1400 and 1407 data (Proctor et al. 2009) are not split by axes. Primed values correspond to a kinematic fit to the Sérsic parameters.

NGC	$n$	$R_e$ ( $''$ )	$\chi^2_{r,1}$	$\chi^2_{r,2}$	$m_{\star,1}$ ( $\times 10^{10} M_\odot$ )	$m_{\star,2}$ ( $\times 10^{10} M_\odot$ )	$n'$	$R'_e$ ( $''$ )	$(\chi^2_{r,1})'$	$(\chi^2_{r,2})'$	$m'_{\star,1}$ ( $\times 10^{10} M_\odot$ )	$m'_{\star,2}$ ( $\times 10^{10} M_\odot$ )
821	4.7	39.8	32.2	13.3	17.8	17.8	8.2	2310.	1.3	2.9	311.	351.
1023	3.9	60.0	3.6	5.1	13.1	11.1	3.1	16.9	0.7	0.9	4.7	3.9
1344	4.1	50.0	84.2	22.2	15.0	12.5	8.3	765.1	8.2	14.7	70.5	68.0
1400 <sup>1</sup>	4.0	26.6	7.9	—	23.7	—	9.4	135.8	1.8	—	43.9	—
1407 <sup>1,2</sup>	8.3	67.4	23.5	—	44.5	—	—	—	—	—	—	—
3377 <sup>2</sup>	5.2	54.0	34.6	19.6	0.2	0.3	—	—	—	—	—	—
3379	4.7	47.0	16.5	4.9	0.9	0.8	8.9	275.9	4.4	2.4	19.2	18.7
3608	7.0	157.0	50.1	49.8	31.0	30.0	3.5	8.9	6.2	7.0	4.3	4.2
4374	8.0	142.0	4.6	6.2	51.4	50.9	8.1	344.6	2.1	2.5	102.0	101.0
4494	3.3	49.0	7.4	7.6	10.5	11.0	7.2	490.5	5.5	2.1	41.2	39.0
4564	3.1	33.8	935.0	572.0	0.7	0.8	2.3	3.4	4.8	22.2	1.0	1.0
4697	3.5	66.0	0.4	2.3	14.5	14.5	5.8	614.3	0.3	1.2	79.5	76.1
5128 <sup>2</sup>	4.0	305.0	7.2	1.3	17.1	16.5	—	—	—	—	—	—
5846	4.0	69.5	7.6	5.8	51.3	51.2	8.1	1039.0	2.3	1.97	263.0	264.0

<sup>1</sup> Only one axis available (data taken over a circular aperture).

<sup>2</sup> In these galaxies, the kinematic fit to the Sérsic parameters does not converge.

**Table 2.** Characteristics of the formally best fits for our stellar + polytropic dark matter model for each galaxy. Columns from left to right are: the galaxy identifier (subscripted with the axis – axis 0 meaning circular annuli); the dark matter thermal degrees of freedom; quality of fit for stars + halo ( $\chi^2_r$ ); quality of fit with stars alone ( $\chi^2_{r,\star}$ ; including PNe data); truncation radius of the halo; stellar mass to light ratio in B band; baryon fraction of the interior ( $r < 1R_e$ ); baryon fraction of middle regions ( $r < 5R_e$ ). The uncertainties are quoted at the  $1\sigma$  level.

NGC	$M_B$	$M_\star \times 10^{10} M_\odot$	$F_d$	$\chi^2_r$	$\chi^2_{r,\star}$	$\log R_h/R_e$	$\Upsilon_\star^B(\leq R_e)/\Upsilon_\odot^B$	$f_B(\leq R_e)$	$f_B(\leq 5R_e)$
821 <sub>(0)</sub>	-20.74	$16.3 \pm 1.0$	7.9	1.9	3.0	6.00	$5.31 \pm 0.32$	$0.80 \pm 0.11$	$0.49 \pm 0.26$
821 <sub>(1)</sub>	-20.74	$12.8 \pm 1.6$	8.0	1.7	26.4	1.97	$4.16 \pm 0.52$	$0.62 \pm 0.12$	$0.25 \pm 0.08$
821 <sub>(2)</sub>	-20.74	$13.6 \pm 2.7$	8.7	1.8	8.9	6.01	$4.42 \pm 0.87$	$0.57 \pm 0.23$	$0.23 \pm 0.33$
1023 <sub>(1)</sub>	-20.92	$0.4 \pm 4.9$	9.9	1.9	2.3	0.84	$0.12 \pm 1.36$	$0.08 \pm 0.39$	$0.14 \pm 0.37$
1023 <sub>(2)</sub>	-20.92	$0.3 \pm 4.9$	9.9	1.1	4.4	0.73	$0.08 \pm 1.35$	$0.07 \pm 0.45$	$0.14 \pm 0.39$
1344 <sub>(1)</sub>	-19.59	$12.1 \pm 0.7$	5.7	2.6	4.8	1.40	$11.32 \pm 0.67$	$0.80 \pm 0.12$	$0.29 \pm 0.30$
1344 <sub>(2)</sub>	-19.59	$13.8 \pm 1.8$	1.6	127.0	111.7	8.88	$12.91 \pm 1.69$	$> 0.82$	$> 0.71$
1400 <sub>(0)</sub>	-20.33	$23.8 \pm 4.1$	0.2	6.5	6.1	2.74	$11.28 \pm 1.93$	$> 0.83$	$> 0.74$
1407 <sub>(0)</sub>	-21.45	$28.5 \pm 2.7$	7.0	0.3	19.8	1.18	$4.82 \pm 0.45$	$0.39 \pm 0.06$	$0.14 \pm 0.02$
3377 <sub>(1)</sub>	-19.16	$0.1 \pm 0.8$	9.9	22.1	25.1	0.32	$0.04 \pm 1.11$	$0.08 \pm 0.41$	$0.14 \pm 0.38$
3377 <sub>(2)</sub>	-19.16	$2.4 \pm 0.9$	0.1	17.5	17.3	0.63	$3.34 \pm 1.31$	$0.87 \pm 0.38$	$0.14 \pm 0.38$
3379 <sub>(0)</sub>	-20.55	$7.5 \pm 0.3$	6.8	1.95	3.25	1.96	$2.91 \pm 0.13$	$0.88 \pm 0.08$	$0.47 \pm 0.26$
3379 <sub>(1)</sub>	-20.55	$8.7 \pm 0.4$	1.7	13.8	11.1	9.46	$3.36 \pm 0.17$	$> 0.90$	$> 0.73$
3379 <sub>(2)</sub>	-20.55	$8.0 \pm 0.3$	0.4	3.3	3.17	1.07	$3.10 \pm 0.11$	$> 0.91$	$0.65 \pm 0.25$
3608 <sub>(1)</sub>	-19.74	$31.3 \pm 5.4$	1.0	50.54	42.8	2.69	$25.53 \pm 4.37$	$> 0.72$	$> 0.64$
3608 <sub>(2)</sub>	-19.74	$30.3 \pm 7.5$	9.9	44.37	42.6	0.19	$24.72 \pm 6.14$	$> 0.68$	$> 0.63$
4374 <sub>(1)</sub>	-21.05	$47.5 \pm 1.1$	8.6	0.1	2.8	3.13	$11.60 \pm 0.28$	$0.59 \pm 0.08$	$0.25 \pm 0.06$
4374 <sub>(2)</sub>	-21.05	$45.6 \pm 2.0$	8.6	0.4	4.4	2.17	$11.14 \pm 0.49$	$0.44 \pm 0.15$	$0.17 \pm 0.14$
4494 <sub>(1)</sub>	-21.02	$10.5 \pm 1.0$	1.6	3.9	4.0	8.88	$2.64 \pm 0.24$	$> 0.90$	$> 0.77$
4494 <sub>(2)</sub>	-21.02	$10.0 \pm 1.4$	1.6	5.9	5.8	8.88	$2.51 \pm 0.36$	$> 0.83$	$> 0.70$
4564 <sub>(1)</sub>	-19.40	$0.1 \pm 0.5$	9.9	3.17	625.8	0.64	$0.13 \pm 0.01$	$0.07 \pm 0.00$	$0.15 \pm 0.05$
4564 <sub>(2)</sub>	-19.40	$0.1 \pm 0.5$	5.0	0.62	370.5	-0.74	$0.09 \pm 0.01$	$0.07 \pm 0.00$	$0.15 \pm 0.06$
4697 <sub>(1)</sub>	-21.15	$13.9 \pm 1.1$	7.4	0.2	0.4	6.23	$3.09 \pm 0.24$	$0.87 \pm 0.09$	$0.67 \pm 0.19$
4697 <sub>(2)</sub>	-21.15	$12.5 \pm 1.8$	8.1	0.5	1.2	6.00	$2.79 \pm 0.39$	$0.75 \pm 0.15$	$0.40 \pm 0.29$
5128 <sub>(1)</sub>	-20.84	$14.3 \pm 1.7$	5.7	0.6	7.1	1.41	$4.24 \pm 0.51$	$0.84 \pm 0.15$	$0.31 \pm 0.14$
5128 <sub>(2)</sub>	-20.84	$14.1 \pm 6.5$	0.1	1.0	1.3	1.12	$4.17 \pm 1.93$	$> 0.58$	$0.71 \pm 0.37$
5846 <sub>(1)</sub>	-21.26	$48.8 \pm 1.4$	0.9	1.0	2.3	0.89	$9.83 \pm 0.28$	$0.94 \pm 0.07$	$0.28 \pm 0.26$
5846 <sub>(2)</sub>	-21.26	$48.5 \pm 1.4$	6.5	0.8	0.7	5.94	$9.78 \pm 0.29$	$0.95 \pm 0.07$	$0.88 \pm 0.24$

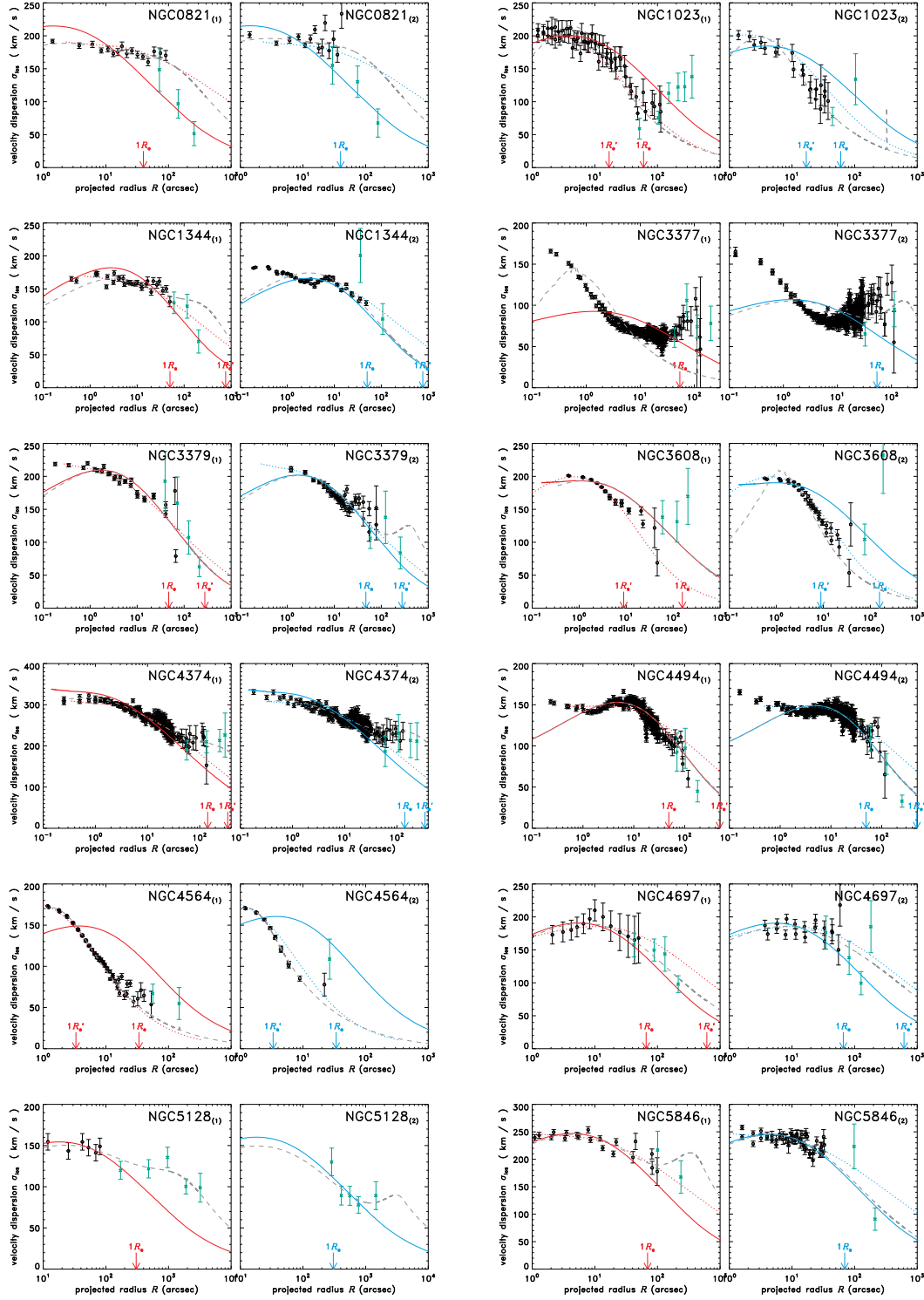


**Figure 1.** Projected velocity dispersion profiles of the isotropic models that best fit the Coccato et al. (2009) data (on two principal axes, red and blue). Stellar data (○) determine these “stars only” fits; the PN (×) data are shown for reference. Solid lines are “stars only” models based on the standard photometric Sérsic parameters; dotted lines reflect parameters adapted to fit the kinematics better. The dashed lines are the best fits of the model including a polytropic dark matter halo. On the horizontal axis, the observed effective radius and the one obtained from the kinematic fit are shown as  $R_e$  and  $R'_e$ , respectively (for some galaxies the “kinematic”  $R_e$  extends beyond the range of the figure, and for three cases (NGC 1407; 3377 and 5128) the kinematic method does not converge; see text for details).



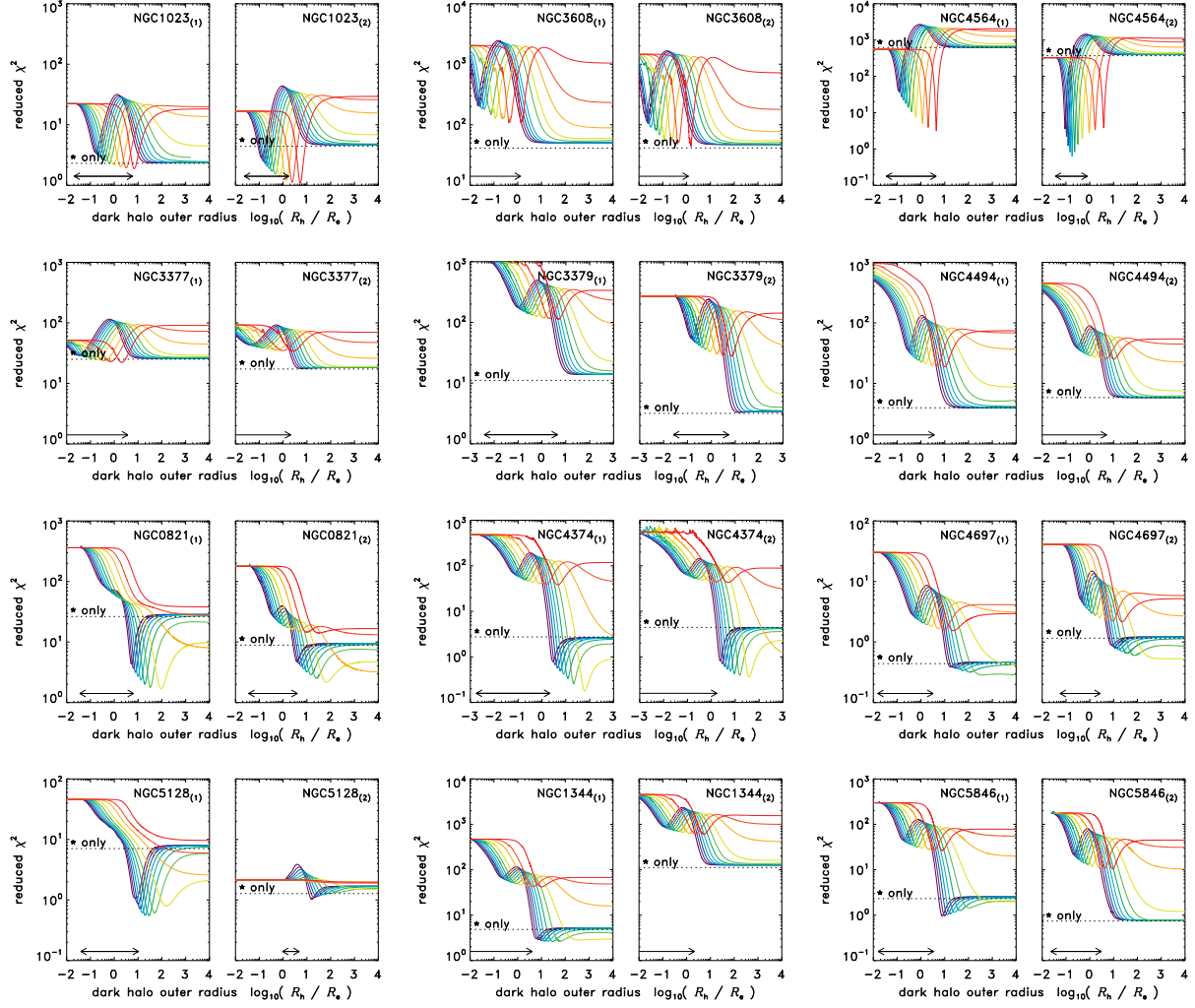


**Figure 2.** Quality of isotropic fits to the Coccato et al. kinematic data for two principal axes, as a function of halo outer radius  $R_h$ . Colours represent cases of different degrees of freedom,  $F_d = 1, 2, 3, 4, 5, 6, 7, 8, 9, 9.5, 9.9$  as indicated in the legend in figure 3. Dotted lines indicate the quality of fit for the Sérsic only model. Arrows show the radial coverage of kinematic data. Stellar data have been softened to a best-fit cubic. Unusually, some of the  $\chi^2$  minima of NGC 1023, 3608 and 4564 imply very compact halos ( $R_h \lesssim R_e$ ) fitting better than the “stars only” level. More plausible fits (lower two rows) prefer a halo radius outside the observed stars and PN.

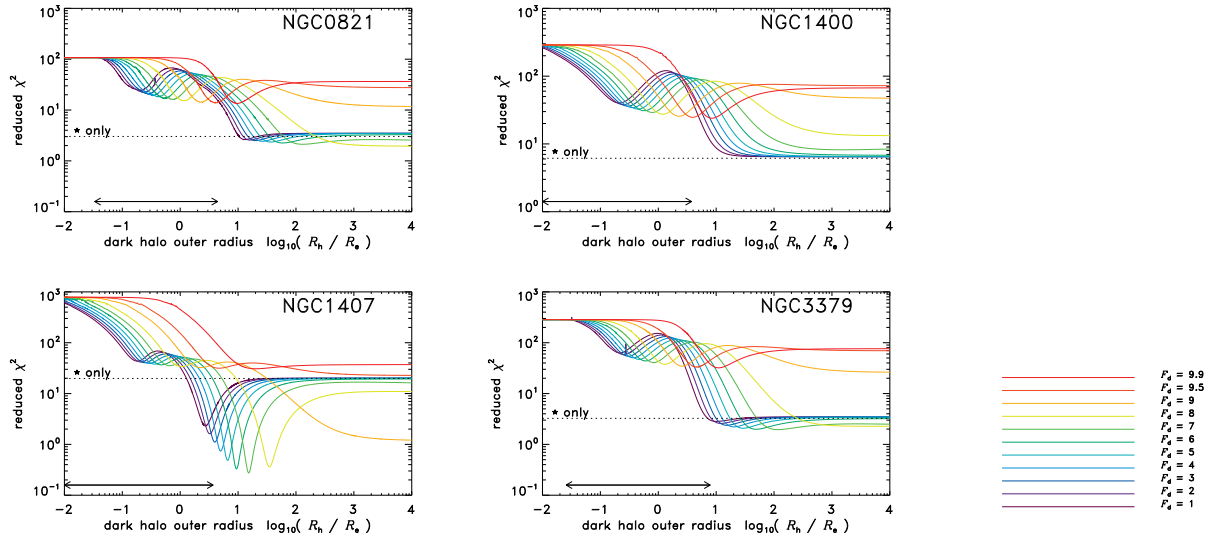


**Figure 3.** Same as figure 2 for data without axial splitting (Romanowsky et al. 2003; Douglas et al. 2007; Proctor et al. 2009).

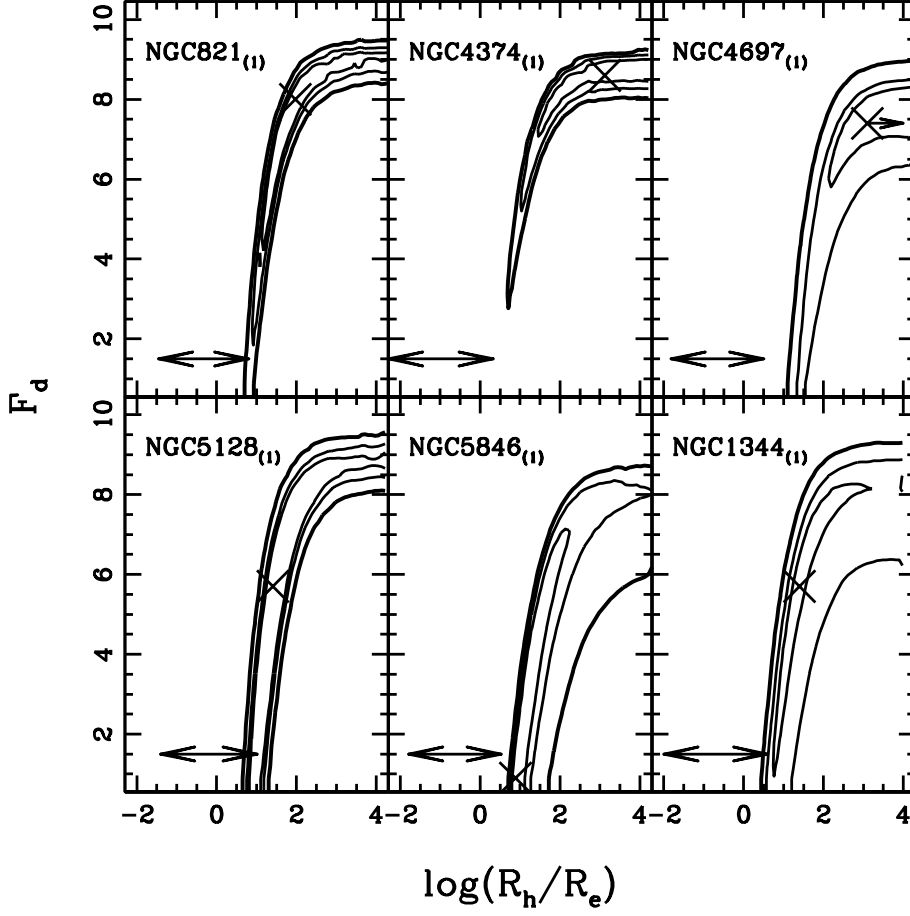


**Figure 4.** The confidence levels in the parameter space spanned by truncation radius ( $R_h$ ; horizontal) and number of degrees of freedom of the dark matter equation of state ( $F_d$ ; vertical) are shown for six of the galaxies from our sample. They correspond to the 90, 95 and 99% (thick like) level, using the likelihood defined by the fit to the velocity dispersion data. The horizontal arrow delimits the range over which the observed data are available. The crosses in each panel give the best fit. Notice the best fit for the truncation radius of NGC 4697 falls outside of the range shown (see table 2).

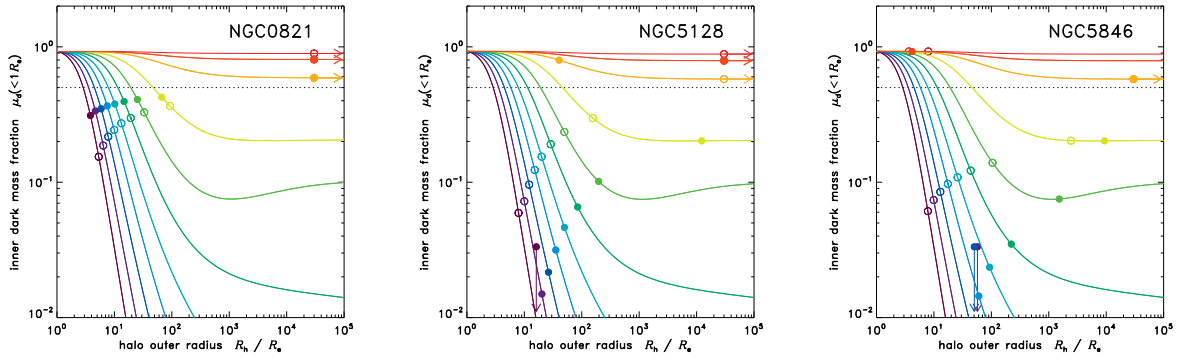


**Figure 5.** The dark mass fraction within  $1R_e$ , as function of halo outer radius, for three galaxies with adequate fits. Open and closed circles mark the best fits to axis 1 and 2 respectively. For  $F_d = 9, 9.5$  and  $9.9$  the dark core outweighs the local stars no matter how far out the halo extends ( $R_h$ ). The horizontal dotted line indicates the regions of baryon-dark matter equality.

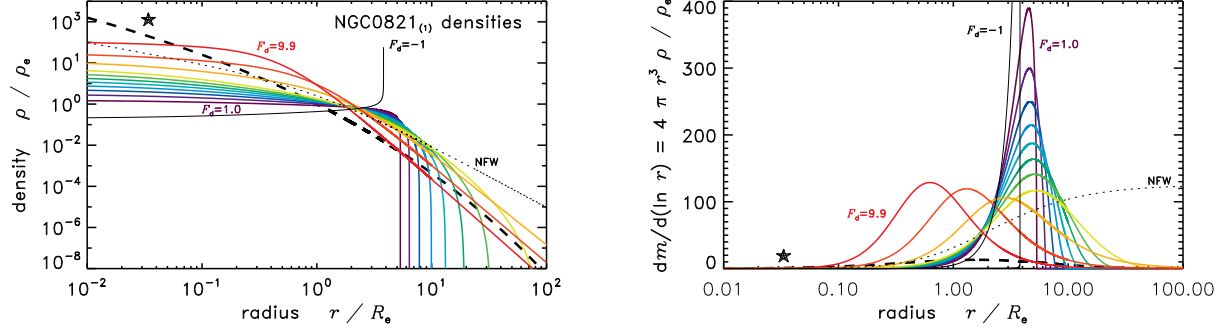


**Figure 6.** The best-fit 3D halo density profiles for NGC 821 (axis 1) data. The first panel shows the  $\rho_d(r)$  curves shaded as usual according to their  $F_d$  values, The dashed black line traces the stellar density profile for comparison. The density normalisation  $\rho_e \equiv \rho_\star(1R_e)$  is obtained in the optimisation of each fit. (The total masses differ between  $F_d$  cases, but the stellar mass fraction is fixed.) The dotted black line corresponds to a standard NFW profile (Navarro et al. 1996). The second panel shows a quantity  $dm_d/d(\ln r)$ , which emphasises the layers where most of the dark mass resides. Visually, the total mass is proportional to the area under each curve. The  $F_d \geq 9$  fits concentrate much of the dark mass within the half-light radius, while  $F_d < 9$  fits concentrate dark mass farther out than several  $R_e$ . The NFW model implies that most of the halo mass resides at the largest radii. We also include a choice of negative  $F_d$  (thin line), which results in an increasing outward density (at decreasing temperature).

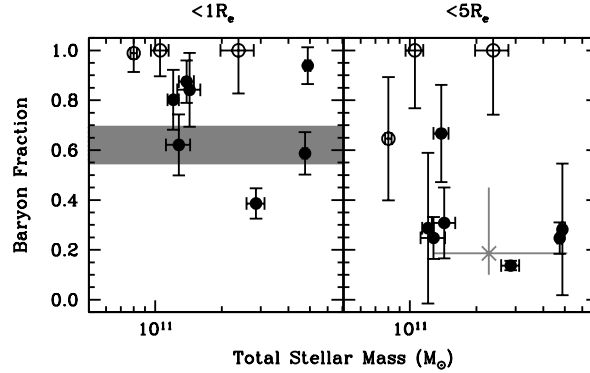


**Figure 7.** The baryon fraction – defined as  $m_\star/(m_\star + m_d)$  is shown within  $1R_e$  (left) and  $5R_e$  versus total stellar mass. We show the best fitting cases that improve over the corresponding “stars only” models. Error bars are shown at the 68% level. The solid dots correspond to galaxies with a good fit  $\chi_r^2 < 3$ . For comparison, the shaded area in the left panel is the result of Bolton et al. (2008) for gravitational lenses in the SLACS survey. The grey cross with 95% error bars is lens B1104-181 from Ferreras et al. (2005), whose lensing and stellar masses are obtained within  $3.7R_e$ .



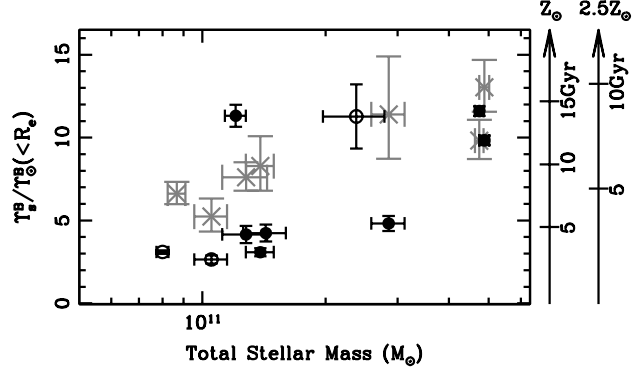


**Figure 8.** The  $B$ -band stellar  $M/L$  ratio is shown versus total stellar mass. The points correspond to the best fitting cases that improve over the corresponding “stars only” models (error bars shown at the 68% confidence level). The solid dots are those galaxies with a  $\chi_r^2 < 3$ . The grey crosses are  $M/L$  values from van der Marel & van Dokkum (2007) for those galaxies that overlap with our sample. The arrows on the right give the stellar  $M/L$  values for a Simple Stellar Population from the CB07 population synthesis models (e.g. Bruzual A 2007) for a Chabrier (2003) IMF. Two metallicities are considered, as labelled.

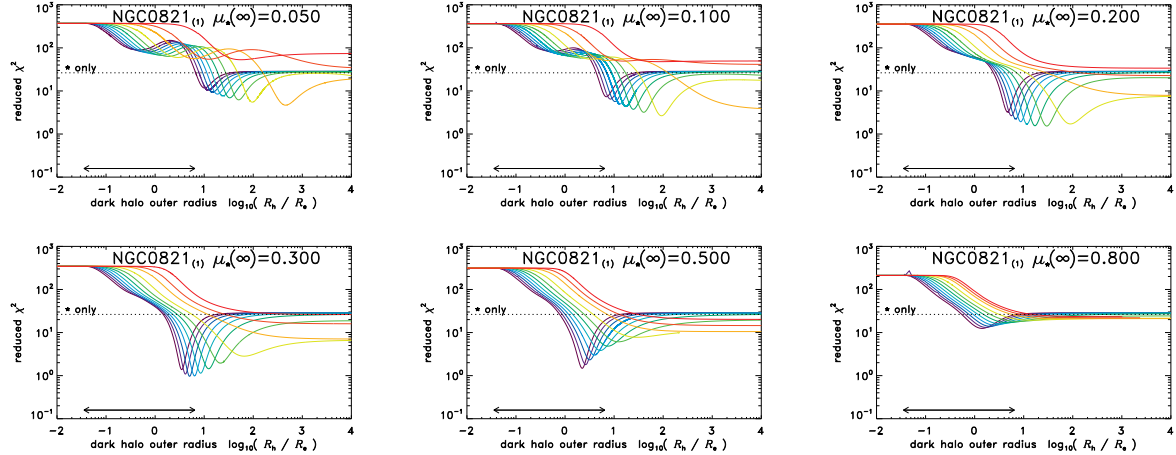


**Figure 9.** Reduced  $\chi^2$  curves for halo models fitted to axis 1 of NGC 821, but with different stellar mass fractions,  $\mu_\star(\infty)$ .

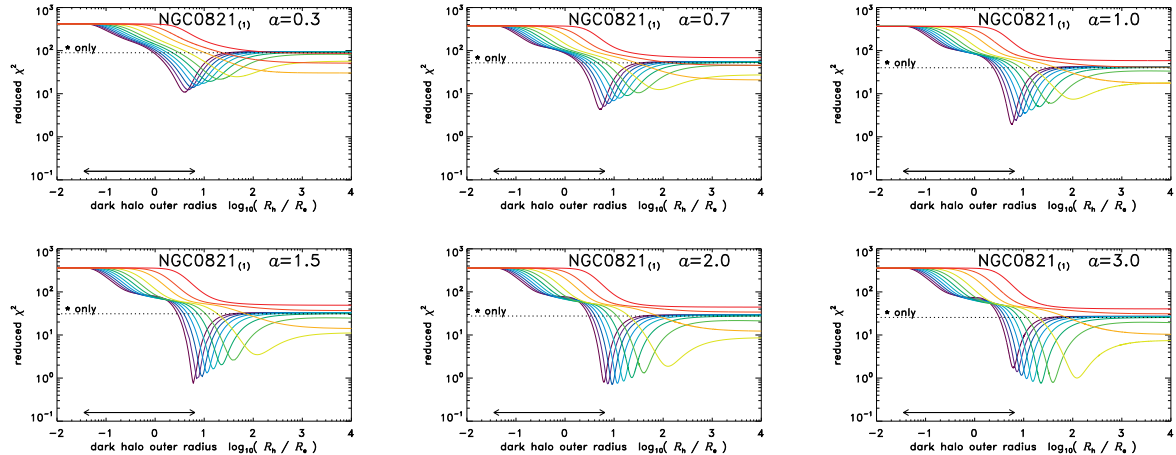


**Figure 10.** Reduced  $\chi^2$  scores of model fits to NGC 821 axis 1, with curves of different  $F_d$  coloured as in Figure 2. Each panel shows a different choice of the Osipkov - Merritt anisotropy scale radius  $a$  (in units of  $R_e$ ).